

Supplemental Information: Sub-femtonewton Force Spectroscopy at the Thermal Limit in Liquids

Lulu Liu,^{1,*} Simon Kheifets,¹ Vincent Ginis,^{1,2} and Federico Capasso^{1,†}

¹*School of Engineering and Applied Sciences, Harvard University, 29 Oxford Street, Cambridge, MA 02138*

²*Applied Physics, Vrije Universiteit Brussel, Pleinlaan 2, 1050 Brussel, Belgium*

MICROFLUIDIC CHAMBERS

Experiments were performed in 25 μm deep microfluidic chambers built on AR coated glass slides. The spacer layer is a closed gasket formed from a rectangular piece of heat-activated sealant sheet (Solaronix Meltonix) with a rectangular channel cut from the center. The top of the chamber is formed by a 60 mm x 25 mm #1.5H glass coverslip. The slide-spacer-coverslip stack is sealed by heating at 100°C under pressure for approximately one minute.

Two small holes are drilled into the coverslip using a laser cutter to permit the inflow and outflow of fluid and microparticles. Two PDMS blocks bonded by plasma oxidation have matching through-holes punched with a 1.5 mm biopsy punch. Fluidic connections into and out of the channel are formed by press-fitting 1/16 inch OD silicone tubing into the PDMS openings. During data acquisition, the inlet and outlet tubes are clamped to minimize fluid flow.

The chamber was mounted on the top prism surface with index-matching oil (Norland 9006) at the interface. The prism and chamber were mounted on a micrometer translation stage to allow for trapping in different parts of the chamber.

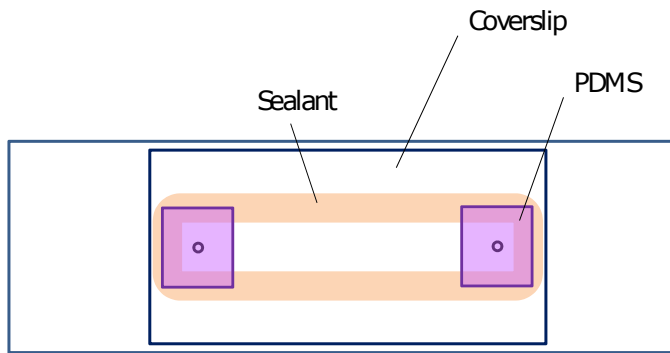


FIG. 1: Top-view of microfluidic chamber.

AR COATING

The AR coating was designed for the trapping wavelength (660 nm), but serves to reduce interference effects not only for the trapping beam but also for the two evanescent fields. The standing wave formed by an optical tweezer focused near a reflective surface results in multiple trapping positions at fixed distances from the surface, preventing the ability to smoothly control the sphere-surface separation. The reflectivity of an uncoated glass-water interface of a tightly-focused Gaussian beam, approximately 0.5%, is large enough to cause this effect, and the AR coating reduces this by a factor of 10, allowing for continuous translation of the trap minimum. The proximity of the pump and probe wavelengths to the AR design wavelength also reduces the effect of multiple scattering of the pump and probe fields [1], allowing us to ignore these higher-order effects.

IMAGING AND ALIGNMENT

Dark field imaging of the trapping region was used to locate particles for trapping, to confirm the presence of trapped particles, and for alignment of the pump, probe, trapping beams and the TIRM detection optics.

A 8% reflective pellicle beamsplitter (Thorlabs BP208) was used to divert light collected by the objective. A 200 mm tube lens was used to image the trapping plane onto a color CCD camera (Thorlabs, DCU224C). For dark field

imaging, a flip-mounted mirror was engaged in order to illuminate the sample with wide-field light from a 150mW, collimated LED (thorlabs, MCWHL2-C2). This white light, dark field image was used to confirm the presence of a trapped particle.

The confocal-like detection of the TIRM signal was aligned by butt-coupling the collection fiber to the 633 nm laser. The steering mirrors between the collection fiber and imaging beam-splitter were aligned such that the reflection of the 633 nm light was collinear with the trapping beam.

The CCD was also used to aid alignment of the two beams entering through the prism. The scattering of the evanescent waves by beads stuck to the surface could be seen on the CCD without LED illumination. The chamber was translated such that a stuck bead was at the center of the trapping beam. The pump and probe beams were aligned to maximize the scattering of evanescent light by that bead.

CALIBRATION PROCEDURE

The calibration procedure follows that found in reference [1]. The addition of salt ensures that the probe particle can be made to approach the surface. In de-ionized water, an electrostatic double layer forms on the surfaces of the glass slide and microsphere, resulting in mutual repulsion at close separation. The addition of the ionic solution reduces the Debye screening length (λ_d) to approximately 1 nm from $\lambda_d \sim 1\mu\text{m}$ for DI water, ensuring accurate calibration of the point of contact. The ionic solution is not used during force measurement as it reduces the trap lifetime by reducing the energy barrier for the microsphere to bind to the surface via van der Waals attraction.

Calibration data for the $2\ \mu\text{m}$ PS bead is shown in figure 2. It is used to determine the constants β , I_0 and C in the relationship $I(z) = I_0 e^{-\beta z} + C$. It is possible that multiple scattering could result in deviation of $I(z)$ from an exponential (adding oscillations with period of $\lambda/2$). However, comparison of numerical simulations for light scattering in our system is against theoretical results ignoring multiple scattering show that this effect is negligible and validate the approximation of an exponential.

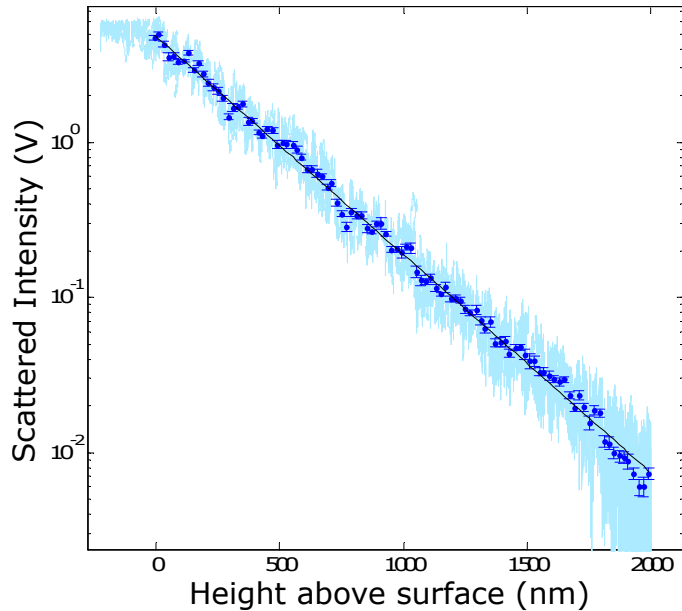


FIG. 2: Calibration data used to convert PD voltage values to absolute separation. Light blue: raw data taken during sweep, where probe particle is stepped towards the surface in 10 nm increments. Dark blue: averaged data. Black line: fit to pure exponential function used to extract the calibration parameters.

PUMP BEAM CHARACTERIZATION

In order to compare force measurements to Mie theory, it is necessary to estimate the intensity of the pump light which undergoes total internal reflection at the glass-water interface below the trapped particle. This estimate is

based on measurement of the (un-chopped) laser power incident on the 60° BK7 prism, P_{in} and measurement of the beam profile of the pump beam.

Beam profile measurement is performed by imaging the surface of a frosted glass slide using a 20× dry microscope objective (Nikon LU Plan Flou). The frosted slide is of approximately the same thickness and the same refractive index as the AR coated slide which forms the bottom of the microfluidic chamber, thus the pump beam propagation matches that of the force measurement experiment. However, the frosted upper surface of the slide (consisting of sub-micron surface roughness) results in scattering of the incident beam to the air above the frosted surface. An image of the scattered light is formed by an objective lens and the CCD camera.

The camera image magnification is calibrated using images of the frosted slide surface when it is translated by a known distance by movement of the micrometer stage on which the prism is mounted.

The beam profile of the scattered light is fit to an elliptical Gaussian distribution with $1/e^2$ beam waists w_x and w_y . The beam entering the prism has a circular Gaussian beam profile, but due to the oblique angle of incidence, the beam as projected onto the chamber surface has a highly elliptical shape.

The intensity at the center of the Gaussian beam, in the plane perpendicular to the propagation direction of the beam, is given by

$$I_0 = \frac{T}{\cos(\theta)} \frac{2P_{in}}{\pi w_x w_y} \quad (1)$$

where $T = 1 - R - l$, R is the Fresnel reflection coefficient for the air-prism interface, l is the propagation loss through 50 mm of BK7, n is the index of the glass, and θ is the angle of incidence on the glass-chamber interface. The factor of $1/\cos(\theta)$ accounts for conversion from intensity on an oblique plane to that of a plane perpendicular to beam propagation.

LOCK-IN ALGORITHM

The lock-in algorithm was implemented using MATLAB and is used to estimate the amplitude and phase of a sinusoidal signal obscured by noise, using a reference signal - in this case the output of the monitor photodiode which records the intensity of the chopper-modulated pump beam.

The first step of the algorithm is to generate a sin wave which is in-phase with the square wave and has unity amplitude. The zero-crossings of the square wave are determined by locating the peaks of the time-derivative of the square wave. These peaks are used to infer the phase as a function of time ϕ_i ; a sawtooth wave with amplitude 2π whose phase matches that of the reference wave.

The noisy (discrete) signal z_i is multiplied by a complex reference signal, $\exp[i\phi_i]$, resulting in the complex lock-in signal $l_i = 2z_i \exp[i\phi_i]$. For times $t_m \gg 2\pi/\omega_L$, the amplitude of the signal is estimated by taking the time-average of the lock-in signal.

In order to correct for the phase delay caused by differences in the signal pathways between the pump monitor photodiode and the TIRM detection photodiode, the delay was directly measured and compensated in the data analysis. This was achieved by removing the 638 nm notch filter in front of the collection fiber for the TIRM signal. A stuck bead was positioned into the detection area, such that the scattered pump light was directly measured by the TIRM photodiode. The pump beam was chopped at several different frequencies, and the collected signal was used to determine the frequency-dependent phase delay between the two signals.

The output of the lock-in algorithm corresponds to the amplitude of the signal at the frequency corresponding to the fundamental frequency of the the square wave with which the pump beam is modulated. The coefficient of the first term of the Fourier series expansion of a square wave is larger than the amplitude of the square wave, by a factor of $\pi/4$. The force we report in our results corresponds to the amplitude of this fundamental component. It is larger than the amplitude of the square wave, but smaller than the peak-to-peak height of the square wave, which corresponds to the DC force of an un-modulated beam, by a factor of $2/\pi$.

FITTING THE MEAN SQUARE DISPLACEMENT

The position power spectral density (PSD), $S_x(w)$, is defined as the Fourier transform of the auto-correlation function $\langle x(t)x(0) \rangle$,

$$S_x(w) = \int_{-\infty}^{\infty} dt e^{i\omega t} \langle x(t)x(0) \rangle \quad (2)$$

The position autocorrelation function is then related to the mean-squared displacement (MSD) by,

$$\text{MSD} = \langle (x(t) - x(0))^2 \rangle = 2\langle x^2 \rangle - 2\langle x(t)x(0) \rangle \quad (3)$$

where $\langle x^2 \rangle$ is the variance of the function $x(t)$.

For a Brownian particle driven by an oscillating force, ignoring inertial effects, the mean square displacement is given by

$$\text{MSD}(t) = \frac{2k_B T}{\kappa} \left[1 - e^{t/\tau_c} \right] + (2A)^2 [1 - \cos(\omega_L t)], \quad (4)$$

where $\tau_c = \gamma/\kappa$.

The damping coefficient γ and trap stiffness κ are extracted from the time-series data using a least-squares fit to the MSD of the Brownian particle. The lock-in amplitude A and frequency ω_L are set to the values determined using the lock-in algorithm described above. Figure 3 shows an example of such a fit. One fit is performed per measurement at a given height.

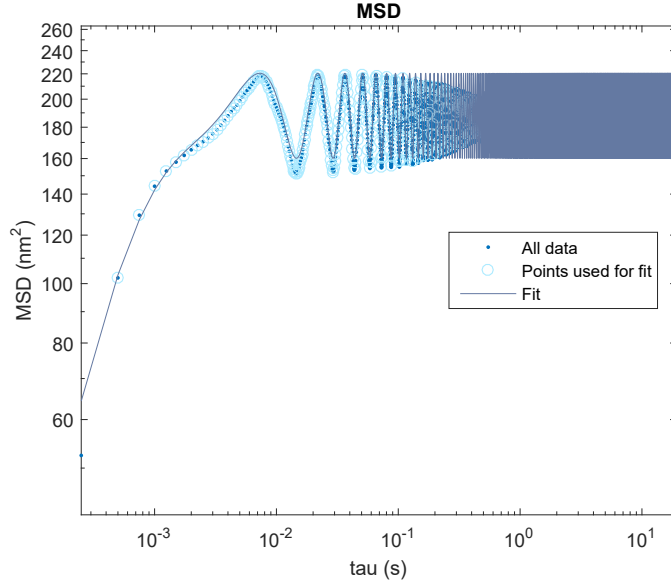


FIG. 3: Fit to MSD of a 2 μm PS particle in fluid. Measurement time is approximately 100 s. The particle is confined in an optical tweezer and driven by a 17 Hz optical force.

HEIGHT-DEPENDENT DAMPING COEFFICIENT

For slow motion of a microscopic sphere in fluid perpendicular to a hard surface with no-slip boundary conditions, Howard Brenner derived an expression for the height-dependent viscous drag, $\gamma(z)$ [2], as correction to the Stokes law result $\gamma_0 = 6\pi\eta R$ in the form of an infinite series. The drag is generally larger than the case with no boundary present due to hydrodynamic coupling between the sphere and the wall. On contact with the wall, the correction coefficient diverges, that is, $\gamma \rightarrow \infty$, and far from the wall, the boundary's influence diminishes and $\gamma(z)$ approaches

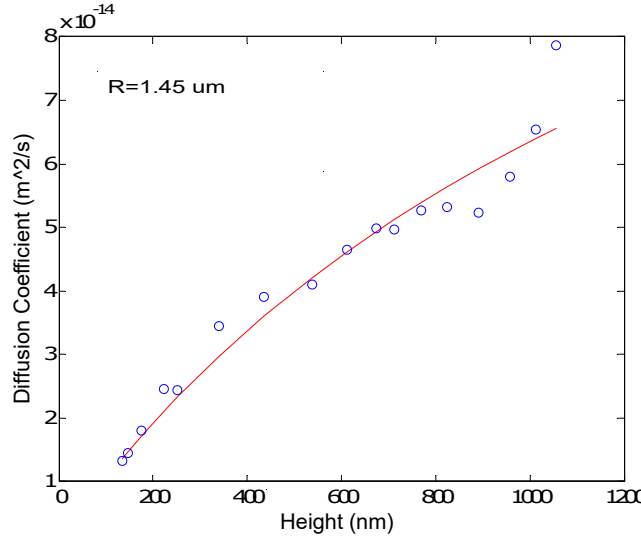


FIG. 4: The measured perpendicular diffusion coefficient as a function of height above surface $D(z)$ for a $2\ \mu\text{m}$ diameter PS microsphere. Best fit to the analytical result described in reference [2] shown in red. Best fit yields a radius of $0.95\ \mu\text{m}$ for the sphere at a temperature of 22C .

that of Stokes law. The diffusion coefficient, which depends inversely on the drag as $D(z) = k_B T / \gamma(z)$, approaches zero for motion in the perpendicular direction as the sphere approaches the wall.

Although the height-dependent damping complicates force measurement, since it results in height dependence of the mechanical susceptibility and the thermal noise, it can also be taken advantage of in order to better estimate the parameters of the system. We perform a fit of the $\gamma(z)$ determined by our MSD fits, to the theory for $D(z)$ of the hindered diffusion model, with the microsphere diameter and point-of-contact as fitting parameters. Although the point of contact can be determined from the calibration scan, this secondary fit provides a more precise estimate. An example of one such fit result is shown in Figure 4.

HEIGHT-DEPENDENT TRAP SPRING CONSTANT

There is also a dependence of the optical tweezer spring constant on the particle's separation from the surface, see Figure 5. This dependence has two contributions.

The first, at intermediate heights above the surface ($\sim 300\text{-}1000\ \text{nm}$), manifests itself as a periodic modulation of the spring constant around some average value, and is due to residual reflection of the trap at the glass-water interface. A more detailed discussion of this effect is available in Section 2: AR Coating. In a sense, by measuring the modulation of the trap stiffness in this manner, we are able to judge the relative effectiveness of our AR coating.

In the second region, at very close separations less than $300\ \text{nm}$ from the surface, the spring constant increases sharply. It is at this height that, typically, the particle's electrostatic repulsion from the surface due to interacting double layers (discussed in Section 4: Calibration Procedure) begins to modify the trap potential. As the particle is brought closer to the surface in this regime, the double layer interaction shifts the equilibrium position of the probe, potentially away from the objective's focus. We can quantify the magnitude of this shift by comparing the expected bead height (assuming it moves in step with the trap focus) with the actual bead height (measured using the calibrated evanescent wave). Usually, when this shift becomes greater than $25\ \text{nm}$, or the typical RMS variation of bead position while trapped, the measurement is stopped. In this way, analytical problems which may arise working with an asymmetric potential are also avoided.

FORCE NOISE SPECTRUM OF A BROWNIAN PROBE

The fluctuation dissipation theorem relates the equilibrium thermal fluctuations of a system to its linear response to an external force. Dissipation of kinetic energy of the probe is mediated by coupling to the many mechanical modes of the fluid. Thermal excitation of these mechanical modes results in the reverse process, transfer of kinetic energy

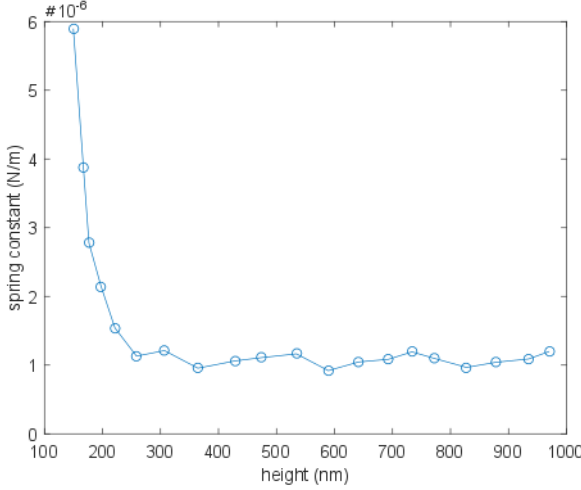


FIG. 5: Fitted trap stiffnesses, κ , in the vertical direction as a function of height. The line is to guide the eye.

from the fluid to mechanical motion of the probe. Both phenomena are mediated by the same mechanism, and in fact the magnitude and dynamics of one can be written in terms of the other.

The response of a probe's motion to an external force can be described by the mechanical susceptibility, $\chi(\omega)$. For a monochromatic force turned on at $t = -\infty$, $F(t) = \Re[F_0 \exp(-i\omega t)]$, the resulting motion of the particle will be at the same frequency, with a phase shift: $x(t) = \Re[\chi(\omega)F_0 \exp(-i\omega t)]$.

The dynamics of a trapped microsphere in fluid can be described by the equation of motion of a damped harmonic oscillator:

$$m\ddot{x} = -\kappa x - \gamma\dot{x} + F_{ext}, \quad (5)$$

where m is the effective mass of the particle, taking into account the inertial mass of the displaced fluid, and changes in velocity are assumed to occur at time scales larger than τ_f , the vortex diffusion time in the fluid, such that the damping force of the fluid can be approximated to respond instantaneously to changes in velocity [3]. The resulting mechanical susceptibility is:

$$\chi(\omega) = \frac{1}{\kappa - m\omega^2 + i\gamma\omega} \quad (6)$$

For timescales longer than τ_c and τ_p , one can neglect the inertial term $m\omega^2$ since it is dominated by the damping and harmonic force.

The statistics of the fluctuations of a stationary process $u(t)$ can be described by the power spectral density (PSD),

$$S_u = 2 \lim_{t_m \rightarrow \infty} \langle \hat{u}_{t_m}(\omega) \hat{u}_{t_m}^*(\omega) \rangle \quad (7)$$

where $\hat{u}_{t_m}(\omega)$ is the truncated Fourier transform of $u(t)$ over time t_m :

$$\hat{u}_{t_m}(\omega) = \int_{-t_m/2}^{t_m/2} u(t) e^{i\omega t} dt \quad (8)$$

and $\langle \dots \rangle$ denotes the expected value over many realizations of the stationary process. The factor of 2 in equation 7 corresponds to the single sided PSD convention; for real $u(t)$, $\hat{u}_{t_m}(\omega) \hat{u}_{t_m}^*(\omega)$ is symmetric in ω , and thus $S^{(1)}(\omega) = S^{(2)}(\omega) + S^{(2)}(-\omega) = 2S^{(2)}(\omega)$ for $\omega \geq 0$, where $S^{(1)}$ and $S^{(2)}$ denote the single- and double-sided PSD, respectively.

The fluctuation dissipation theorem relates the mechanical susceptibility $\chi(\omega)$ of the particle to the thermal fluctuations of its position, $S_x^{th}(\omega)$ or of the thermal force which drives those fluctuations, $S_F^{th}(\omega) = S_x^{th}(\omega) |\chi(\omega)|^{-2}$:

$$S_x^{th}(\omega) = \frac{4k_B T}{\omega} \text{Im}[\chi(\omega)] \quad (9)$$

$$S_F^{th}(\omega) = \frac{4k_B T}{\omega} \text{Im} \left[\frac{1}{\chi(\omega)} \right]. \quad (10)$$

The resulting single-sided thermal noise PSD for our system is $S_F^{th}(\omega) = 4\gamma k_B T$. In the case that time-dependent damping must be taken into account, which is the case for velocity fluctuations at time scales on the order of τ_f , the damping term has frequency dependence and the thermal force deviates from that of flat white noise.

NOISE IN A DC FORCE MEASUREMENT

The effect of a low pass filter on a signal $x(t)$ can be written as a convolution with a window function $B(t)$

$$w(t) = x(t) \otimes B(t) \quad (11)$$

It can be shown that the variance of a low-pass filtered signal is

$$\text{var}(w) = \int_0^\infty |\hat{B}(\omega)|^2 S_x \frac{d\omega}{2\pi}, \quad (12)$$

Where $\hat{B}(\omega)$ is the Fourier transform of the window function, while S_x is the power spectral density of the un-filtered signal.

If $B(t)$ is a rectangular window function with width t_m and area 1, then $\hat{B}(\omega) = \text{sinc}(\omega t_m/2)$. For an unfiltered variable with a white noise PSD, $S_x(\omega) = S_x(0)$, the variance of w will be $S_x(0)/2t_m$.

In the case of a DC force measurement with an over-damped compliant probe, the signal is $F = \kappa x_{avg}$, while the noise, given as the standard deviation of repeated measurements is $\sigma_F = \kappa \sqrt{\text{var}(x_{avg})}$. In the presence of only Brownian motion noise, if averaging time t_m is such that the measurement bandwidth $2\pi/t_m$ is below the corner frequency $\omega_c = \gamma/\kappa$, the white noise approximation is valid in the frequency range selected by the filter, and thus the thermal noise will be $\sigma_F = \sqrt{2\gamma k_B T/t_m}$.

While the thermal force noise spectrum is effectively frequency independent, low frequency technical noise sources are almost impossible to eliminate. $1/f$ noise can contribute orders of magnitude more noise than the thermal limit, and cannot be eliminated by a low-pass filter.

NOISE IN A LOCK-IN FORCE MEASUREMENT

In a lock-in measurement, an oscillating force is applied to the probe:

$$F(t) = F_0 \sin(\omega_l t) \quad (13)$$

resulting in motion of the particle

$$x(t) = x_0 \sin(\omega_l t + \theta) + x_n \quad (14)$$

where $x_0 = F |\chi(\omega_l)|$, $\theta = \arg(\chi(\omega_l))$, and x_n is the thermal (non-deterministic) component of the motion of the particle.

The in-phase lock-in signal is determined by low-pass filtering the lock-in signal $l(t)$, where

$$l(t) = 2x(t) \sin(\omega_l t + \theta) \quad (15)$$

The low-passed lock in signal, $L(t) \equiv l(t) \otimes B(t)$, has mean of x_0 . Writing $l(t) = l_s + l_n$, where $l_s = 2x(t) \sin^2(\omega_l t + \theta)$ and $l_n = 2x_n \sin(\omega_l t + \theta)$, the standard deviation of L can be found by determining S_{l_n} , the PSD of the random component of $l(t)$.

The PSD of l_n can be written in terms of the PSD of x_n . By noting

$$l_n = x_n (e^{i\omega_l t + i\theta} + e^{-i\omega_l t - i\theta}) \quad (16)$$

It follows that the Fourier transform of l_n is

$$\tilde{l}_n = e^{i\theta} \tilde{x}_n(\omega - \omega_l) + e^{-i\theta} \tilde{x}_n(\omega + \omega_l) \quad (17)$$

The PSD becomes

$$S_{l_n} = 2\tilde{l}_n \tilde{l}_n^* = S_x(\omega + \omega_l) + S_x(\omega - \omega_l) \quad (18)$$

The two cross terms vanish because x_n is a stationary process. The variance of the lock-in force measurement is

$$\text{var}(L) = S_{l_n}(\omega = 0)/2t_m = S_x(\omega_l)/t_m. \quad (19)$$

Thus it follows that the standard deviation of the force is

$$\sigma_F = \sqrt{4\gamma k_B T/t_m} \quad (20)$$

NOISE IN A PFM FORCE MEASUREMENT

Photonic force microscopy (PFM) takes advantage of the result of Boltzmann statistics and the ergodic theorem to relate the distribution of points in space visited along a Brownian particle's trajectory to the local potential energy landscape. In the one-dimensional case, this is given by

$$p(z) = C \exp \left[\frac{-V(z)}{k_B T} \right] \quad (21)$$

where $p(z_i)dz$ is the fraction of time spent within the region $z_i < z < z_i + dz$, $V(z)$ is the position-dependent potential energy, and C is a normalization constant.

The probability density is estimated from a recorded, discretized trajectory of Brownian motion, consisting of consecutive samples z_i of the average position of the particle during time interval $t_i < t < t_{i+1}$ of duration $t_{i+1} - t_i = \tau_s$. The result is a histogram N_j , where N_j is the number points along the trajectory which lie between $z_j < z < z_{j+1}$. This is used to estimate a discretized probability density, $p_j \Delta z = N_j/N_{tot}$, where N_{tot} is the total number of position samples, p_j is the average of $p(z)$ for $z_j < z < z_{j+1}$ and Δz is $z_{j+1} - z_j$. The potential energy landscape is then determined by equation 21:

$$V_i = k_B T [\log(p_i) + \log(C)], \quad (22)$$

where C is an arbitrary offset. The force field is then estimated by numerical spatial differentiation of V_i . The simplest method is to use the single-point derivative, resulting in

$$F_i = \frac{V_{i+1} - V_i}{\Delta z}, \quad (23)$$

where F_i is the spatial average of $F(z)$ between z_i and z_{i+2} .

For many repeated trajectories of duration t_m , the experimental histograms N_j will fluctuate about the mean value. In the case that the consecutive z_i are uncorrelated, the variance of N_j will be given by $\sqrt{N_j}$. This is the case if the averaging time is much larger than the correlation time of the position fluctuations of Brownian motion $\tau_k \equiv \gamma/\kappa$. If the averaging time is smaller than τ_k , consecutive position samples will be correlated; the rate of acquisition of information about the potential landscape will be limited not by the experimental sampling rate but by the rate at which the particle samples new regions of space. As a result, the variance in each histogram bin will be larger than $\sqrt{N_j}$, approaching $\sqrt{N_j \tau_s / \tau_k}$ for $\tau_s \ll \tau_k$. We have

$$N_j = N_{tot} p_j \Delta Z \quad (24)$$

and

$$N_{tot} = t_m / \tau_s \quad (25)$$

which gives the relative error on each p_j

$$\frac{\Delta p_j}{p_j} = \frac{\Delta N_j}{N_j} = \sqrt{\frac{\tau_k}{t_m p_j \Delta Z}} \quad (26)$$

where we note that the denominator inside the square root is the fraction of time spent by the particle inside the measurement volume. This propagates to an absolute error in V_j , according to equation 22, of

$$\Delta V_j = k_B T \frac{\Delta p_j}{p_j} = k_B T \sqrt{\frac{\tau_k}{t_m p_j \Delta z}} \quad (27)$$

and thus an error of the force of equation 23 of

$$\Delta F_j = \frac{2k_B T}{\Delta z} \sqrt{\frac{\tau_k}{t_m p_j \Delta z}} \quad (28)$$

In PFM force measurement there is a tradeoff between position resolution and force sensitivity. The uncertainty in the force measured by PFM scales as $\Delta z^{-3/2}$, where Δz is the width of each histogram bin and the position resolution of the force. The highest force sensitivity is achieved by defining only two histogram bins (and thus one single force measurement averaged over the entire trapping volume) and choosing Δz near $z_{th} = \sqrt{k_B T / \kappa}$ (the rms width of the probability distribution of the trapped particle's thermal motion). In this case, $p_j \Delta z$ approaches 1/2, and $\Delta F = 2\sqrt{2\gamma k_B T / t_m}$. Thus, the best force sensitivity achievable using PFM is comparable to that of DC or AC single-point force measurement.

For a given trap, PFM provides a method to resolve the spatial dependence of forces at length scales far smaller than z_{th} , given sufficient measurement time or sufficiently strong forces. However, in some situations it may be advantageous to instead increase the trap stiffness (thus reducing z_{th}) and perform several single-point measurements while scanning the trap position.

In the former case, an N -point force measurement performed with spatial resolution of $\Delta z = z_{th}/N$ will have an average uncertainty of $N^{3/2} \sqrt{4\gamma k_B T / t_m}$. In the latter case, N consecutive measurements, each with duration t_m/N , will each have a force uncertainty of $N^{1/2} \sqrt{8\gamma k_B T / t_m}$ – an N -fold improvement of SNR.

DETAILS OF THE ANALYTICAL CALCULATIONS USING MIE THEORY

The sizes of particle in our experiment are comparable to the wavelength of the incident light. Therefore, we cannot resort to the Rayleigh approximation or ray theory, but rather need to use full Mie theory to calculate the optical force acting upon the spheres. In general, one would need to calculate the total field surrounding the dielectric particle, i.e., the incident and the scattered/reflected field from the particle, and subsequently integrate the Maxwell stress tensor to obtain the optical force that acts upon the sphere. However, this approach is computationally extremely complex and only converges very slowly. Therefore, Barton et al. integrated the Maxwell stress tensor as a function of general Mie scattering coefficients. In this way, they developed a method that allows for the calculation of the optical forces using an algebraic combination of the Mie scattering coefficients. Following their algorithm, the time-averaged attractive force (towards the surface) was calculated using

$$\begin{aligned} \frac{\langle F_z \rangle}{a^2 \epsilon_0 E_0^2} = & \operatorname{Re} \frac{i\alpha^2}{4} \sum_{l=1}^{\infty} \sum_{m=-l}^l \sqrt{\frac{(l+m+2)(l+m+1)}{(2l+1)(2l+3)}} l(l+2) \\ & \times (2n_w^2 a_{l,m} a_{l+1,m+1}^* + n_w^2 a_{l,m} A_{l+1,m+1}^* + n_w^2 A_{l,m} a_{l+1,m+1}^* \\ & + 2b_{l,m} b_{l+1,m+1}^* + b_{l,m} B_{l+1,m+1}^* + B_{l,m} b_{l+1,m+1}^*) \\ & + \sqrt{\frac{(l-m+1)(l-m+2)}{(2l+1)(2l+3)}} l(l+2) \\ & \times (2n_w^2 a_{l+1,m-1} a_{l,m}^* + n_w^2 a_{l+1,m-1} A_{l,m}^* + n_w^2 A_{l+1,m-1} a_{l,m}^* \\ & + 2b_{l+1,m-1} b_{l,m}^* + b_{l+1,m-1} B_{l,m}^* + B_{l+1,m-1} b_{l,m}^*) \\ & - \sqrt{(l+m+1)(l-m)} n_w \\ & \times (-2a_{l,m} b_{l,m+1}^* + 2b_{l,m} a_{l,m+1} - a_{l,m} B_{l,+1}^* \\ & + b_{l,m} A_{l,m+1}^* + B_{l,m} a_{l,m+1}^* - A_{l,m} b_{l,m+1}^*). \end{aligned} \quad (29)$$

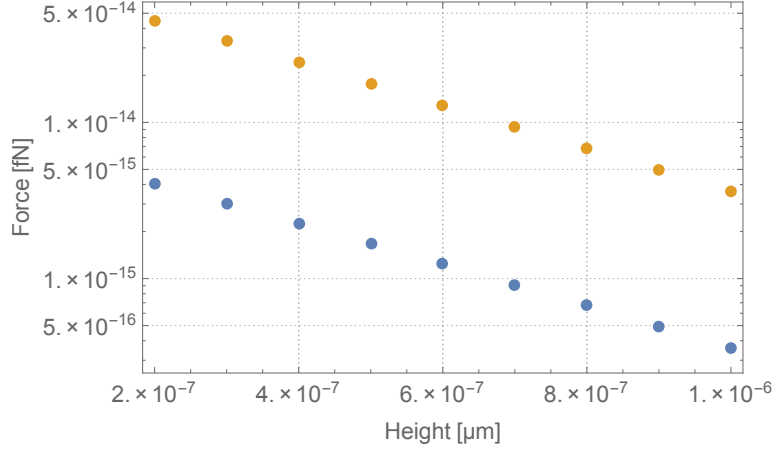


FIG. 6: The numerically simulated attractive force (log scale) as a function of height above the surface for a 2 μm (orange) and a 1 μm (blue) diameter PS microcylinder. The exponential decay of the force confirms that there is no contribution of multiple reflected waves between the surface and the particles.

The Mie scattering coefficients $A_{l,m}$, $B_{l,m}$, $a_{l,m}$ and $b_{l,m}$ in the previous equation are related to the incident (superscript (i)) and the scattered (superscript (s)) fields and are defined by:

$$E_r^{(i)} = \frac{a^2 E_0}{r^2} \sum_{l=1}^{\infty} \sum_{m=-l}^l l(l+1) A_{l,m} \psi_l(n_w k_0 r) Y_{l,m}(\theta, \phi), \quad (30)$$

$$H_r^{(i)} = \frac{a^2 H_0}{r^2} \sum_{l=1}^{\infty} \sum_{m=-l}^l l(l+1) B_{l,m} \psi_l(n_w k_0 r) Y_{l,m}(\theta, \phi), \quad (31)$$

$$E_r^{(s)} = \frac{a^2 E_0}{r^2} \sum_{l=1}^{\infty} \sum_{m=-l}^l l(l+1) a_{l,m} \xi_l^{(1)}(n_w k_0 r) Y_{l,m}(\theta, \phi), \quad (32)$$

$$H_r^{(s)} = \frac{a^2 H_0}{r^2} \sum_{l=1}^{\infty} \sum_{m=-l}^l l(l+1) b_{l,m} \xi_l(n_w k_0 r) Y_{l,m}(\theta, \phi), \quad (33)$$

where a is the radius of the spherical particle, $Y_{l,m}(\theta, \phi)$ are the spherical harmonics, $\psi_l(r) = r j_l(r)$ with $j_l(r)$ the spherical Bessel function, and $\xi_l(r) = r h_l^{(1)}(r)$ with $h_l^{(1)}(r)$ the spherical Hankel function of the first kind.

The value of these scattering coefficients was determined using a traditional Mie scattering algorithm and the infinite series was truncated at a value l for which the relative magnitude of the optical force contribution dropped below 10^{-7} .

FINITE-ELEMENTS NUMERICAL SIMULATIONS

A central assumption in the preceding calculation is that the effect of back-reflected waves between the surface and particle are negligible to the magnitude of the optical force. This assumption was verified using two-dimensional finite-elements numerical simulations (COMSOL multiphysics). In a rectangular simulation domain, an evanescent wave was excited using a plane monochromatic wave that propagates at an angle of 62° and total internally reflects at the interface between the prism—with AR coating—and the surrounding water. The intensity of the incident wave was normalized using the intensity extracted from the experiment and the simulation domain was terminated using perfectly matched boundary conditions that absorb the scattered fields without reflection. In order to avoid enhancement of the evanescent tails inside the perfectly matched layers, the width of the simulation domain was set at 15 μm .

The optical force that acts upon the dielectric particle was evaluated at different heights using the Maxwell Stress tensor formalism. The numerically retrieved attractive forces are shown in figure 6. The exponential decay of the forces with distance confirms the fact that multiple reflected waves do not contribute to the total force in our setup.

Indeed, multiple reflections typically generate deviations from the exponential decay of the force as a function of the height. These results justify the assumption to neglect multiple reflections in the analytical calculations.

* Email: lululiu@fas.harvard.edu

† Email: capasso@seas.harvard.edu

- [1] L. Liu, A. Woolf, A. W. Rodriguez, and F. Capasso, Proceedings of the National Academy of Sciences **111**, E5609 (2014), ISSN 0027-8424, URL <http://www.pnas.org/lookup/doi/10.1073/pnas.1422178112>.
- [2] H. Brenner, Chemical Engineering Science **16**, 242 (1961).
- [3] S. Kheifets, A. Simha, K. Melin, T. Li, and M. G. Raizen, science **343**, 1493 (2014).